Multi-layer solar selective absorber coatings based on W/WSiAlNx//WSiAlOyNx/SiAlOx for high temperature applications

A. AL-Rjoub[a,1], L. Rebouta[a], P. Costa[a], L. G. Vieira[b]

a Centre of Physics, University of Minho, Campus de Azurém, 4800-058 Guimarães, Portugal
b Centre of Physics, University of Minho, Campus de Gualtar, 4710-057 Braga, Portugal

Abstract

A simulated and an experimental design of multilayer solar selective absorber for high temperature applications is presented in this study. The optical tandem is composed of four layers deposited by magnetron sputtering on stainless steel substrates at room temperature. The first is a back-reflector tungsten layer, that is followed by two absorption layers, based on $WSiAlN_x$/ $WSiAlO_yN_x$ structure, for phase interference. The final layer is an antireflection layer of $SiAlO_x$. The design was conducted with the help of SCOUT software creating a model multilayer based on transmittance and reflectance spectra of individual thin layers deposited on glass substrates. The final design shows simultaneously high solar absorptance α= 96.0 % and low emissivity ε= 10.5% (calculated at 400 ºC) together with high thermal stability at 450 ºC, in air, and 600 ºC in vacuum for 400h and 300 h, respectively.

Keywords: solar selective absorber, optical constants, sputtering, $WSiAlN_x$ /$WSiAlO_yN_x$

1. Introduction

Structures based on transition metal nitrides and oxynitrides are one of the most used metal in selective solar thermal absorber stacks because of their high thermal stability, high oxidation resistance, good diffusion barrier and excellent selectivity. Such stacks can be used in the concentrated solar power (CSP) technology, that uses a parabolic-trough solar systems to improve energy absorption and employing it in steam turbines to produce electricity or in other applications [1][2][3]. However, any absorber tandem should be highly efficient in terms of selectivity, that is, it should have a high absorptance (α) at solar radiation region (wavelength range of 0.3- 2.0 µm), and a low thermal emittance in IR region (wavelength range dependent on temperature application, but usually greater than 2.0 µm). Superior selectivity can be achieved if the multi-layer absorber tandem has a decreasing refractive index and extinction coefficient from substrate to surface, which can be easily obtained by

---

appropriate choice of layers thicknesses and material composition. In the ideal case, at the front of the solar absorber, in the antireflection layer, n and k should be 1 and 0, respectively.

The most used transition metals are Ti [4][5][6][7], Cr [8], W [9], Nb [10], and Al [11] or combination between them. Most of these designs showed a good thermal stability and good oxidation resistance and share the same structure of general design as substrate (i.e. stainless steel) \ back reflector metal (i.e. W) \ metal nitride \ metal oxynitride\ oxide layer as antireflection layer.

In the previous study, a design of solar absorber tandems based on AlSiOx:W cermets with high (HA) and low (LA) metal volume fraction (W/AlSiO$_x$:W(HA)/AlSiO$_x$:W(LA)/AlSiO$_x$,) [35] and based on nitride/oxynitride layers (W/CrAlSiN$_x$/CrAlSiO$_y$N$_x$/SiAlO$_x$) [***include ref submitted***] were studied and fully illustrated. The final design showed simultaneously a high solar absorbance $\alpha \approx$ 95 % and low emissivity ε= 10-12 % (at 400 ºC) together with high thermal stability at 450 ºC and 400 ºC, in air, and 580 ºC and 600 ºC in vacuum, respectively. With the current work, also based on nitride/oxynitride structure, the transition metal chromium was replaced with tungsten and the result was excellent. So, this work presents a new design of solar selective absorber for high temperature applications, with structure (W/WSiAlN$_x$ /WSiAlO$_y$N$_x$/SiAlO$_x$).

2. Materials and methods

2.1 Coatings deposition

All Films were deposited by dc magnetron sputtering onto p-doped Boron Si (100) (used for Scanning Electron Microscopy (SEM) and X-Ray Photoelectron Spectroscopy (XPS) analyses), glass (used for tracing the optical properties of single layers) and polished stainless steel (AISI304) substrates (used for Energy Dispersive X-ray Spectroscopy (EDS) analyses, X-ray diffraction(XRD) and accelerated lifetime thermal tests of resulting tandems). The depositions were performed using a substrate holder placed 9 cm above the target and working in static mode. Tungsten layers were deposited using a tungsten target (99.99%) with a diameter of 10 cm. Then, the same target was used to deposit WSiAlN$_x$ and WSiAlO$_y$N$_x$ layers, by adding 9 silicon pellets with a diameter of 10 mm and 9 squares of aluminum pieces with 1 cm ×1 cm on the target erosion zone. For SiAlO$_x$ oxide layer, a Si80 Al20 target was used, with oxygen as a reactive gas.

All layers were deposited in similar conditions by dc magnetron sputtering (P_{Ar}=0.37 Pa, current density 6.4 mA/cm^2, pulsed bias of -60 V, f =90 kHz, room temperature and base pressure 2×10^{-4} Pa), except in tungsten layer case, in which the current density was 12.7 mA/cm^2. Silicon and stainless steel substrates were ultra sound cleaned in acetone for 15 min, and ion etched before the deposition. During the target cleaning process, the substrates were protected by a stainless steel shield.

2.2 Coatings' chemical composition, bonding, structure and morphology

The coatings' chemical composition of thick individual layers was assessed by means of EDS analyses. The measurements were performed on randomly selected regions of the sample surface with an acceleration voltage of 7 keV. Scanning electron microscopy analysis was performed in a NanoSEM-FEI Nova 200 (FEG/SEM) equipment, to determine the coatings thickness and morphology.

For structural and oxidation resistance studies, glancing incidence angle XRD was used for single layers and for tandem before and after annealing, performed by employing a Bruker AXS Discover D8 operating with Cu Kα radiation. The measurements were performed at fixed incidence angle of α = 3º.

The chemical bonding state of thick WSiAlNx and WSiAlOyNx single layers (similar to those used in multilayer stack) was evaluated using X-Ray Photoelectron Spectroscopy (XPS) analysis. XPS was performed in a Kratos AXIS Ultra HAS X-Ray Photoelectron Spectroscopy system from Centro de Materiais da Universidade do Porto (CEMUP), using an Al Kα (1486.7 eV) X-Ray source, with a 40 eV pass energy. The C1s line at 285.0 eV was used to calibrate the binding energies. The XPS spectra were analyzed in CasaXPS software[12], and all peaks were fitted using a Shirley background and GL (30)^2 line shape. For W 4f core level, fittings were done assuming the peak doublets with spin-orbit separation (ΔE_P) $4f_{5/2} - 4f_{7/2} = 2.18$ eV and with peaks' intensity ratio $I_{W\,4f_{5/2}}/I_{W\,4f_{7/2}} = 0.75$. In some cases, it

---

^{2} GL (p): Gaussian/Lorentzian product formula where the mixing is determined by m = p/100, GL (100) is a pure Lorentzian whereas GL (0) is pure Gaussian.

was necessary to involve $W\,5p_{3/2}$ at higher binding energy (BE) side of $4f_{5/2}$ with $BE_{W\,5p_{3/2}} = BE_{W\,4f_{7/2}} + 5.8$ and $I_{W\,5p_{5/2}}/I_{W\,4f_{7/2}} = 0.08$ [13].

2.3 Thermal treatment of the absorber tandem

The optical stack was subjected to annealing tests in air at 450 ºC and in vacuum at 600 ºC for 400 h and 300 h, respectively. According to vacuum annealing, the furnace was evacuated to the base pressure of 5.0 mPa and annealing was performed for three steps 150 h, 100 h and 50 h, respectively. After each step, the vacuum was broken, and the reflectance of samples was measured to evaluate the absorptance and the emissivity. On the other hand, the steps for air annealing were 150 h and 250 h.

2.4 Characterization of optical properties and SCOUT simulation

The transmittance (T) and the reflectance(R) of individual thin layers of $WSiAlN_x$, $WSiAlO_yN_x$, W and $SiAlO_x$ deposited on glass substrate were measured by using a Shimadzu PC3100 spectrophotometer, in the wavelength range of 0.25 – 2.5 µm. The reflectance data were obtained at quasi-normal incidence (angle of incidence of 8º) using an Al mirror as reference. The results were used to calculate the optical constants (refractive index n and extinction coefficient k), n and thicknesses, by using the software SCOUT[14] to simultaneously fit an optical model to the transmittance and reflectance spectra of each individual layer. SCOUT allows to perform a standard spectrum simulation employing the Fresnel equations together with appropriate models for the frequency dependent complex dielectric function ($\tilde{\varepsilon}_r = \varepsilon_1 + i\varepsilon_2$) To model $\tilde{\varepsilon}_r$ we have considered a sum of several contributions as shown in equation (1)

$$\tilde{\varepsilon}_r = \varepsilon_{back\,ground} + \tilde{\varepsilon}_{Drude} + \sum \tilde{\varepsilon}_{Lorentz} + \tilde{\varepsilon}_{OJL} \quad (1)$$

where $\varepsilon_{back\,ground}$, $\tilde{\varepsilon}_{Drude}$, $\tilde{\varepsilon}_{Lorentz}$ and $\tilde{\varepsilon}_{OJL}$ are real high frequency dielectric constant, Drude model (free carriers contribution), harmonic Lorentz oscillators (bound charges contribution) and OJL model (that accounts for other interband transitions), respectively [15][16]. Notice that all these models use causal quantities to describe the dielectric function, including the OJL model that is specifically modified

in the SCOUT software to ensure the Kramers-Kronig compatibility between the real and imaginary parts of the dielectric function. Then, the complex refractive index ($\tilde{n}$) can be calculated from the relation $\tilde{n}^2 = (n + ik)^2 = \tilde{\varepsilon}_r$.

The first step was to measure and model the reflectance and transmittance spectra of the glass substrate to extract its optical constants. These quantities were later used in the simulation of the spectra of each layer deposited on a similar substrate. Based on results obtained from individual layers, the final tandem of thermal absorber was also optimized by SCOUT.

The normal solar absorptance (α_s) was determined from equation (2) by calculated or experimental spectral reflectance data $R(\lambda)$ and ASTM AM1.5D solar spectral irradiance, $I_s(\lambda)$ (*** INCLUDE REFERENCE***), at the wavelength range of $0.3 - 2.5$ μm.

$$\alpha_{sol} = \frac{\int_{0.3\mu m}^{2.5\mu m} I_s(\lambda)[1-R(\lambda)]\, d\lambda}{\int_{0.3\mu m}^{2.5\mu m} I_s(\lambda)\, d\lambda} \qquad (2)$$

The infrared specular reflectance spectra were measured in the wavelength range of 2–25 μm (wavenumber range $5000 - 400$ cm^{-1}) at near normal incidence (angle of incidence $\alpha \approx 11°$) with a Fourier Transform Infrared spectrometer Bruker IFS 66V equipped with a globar source, a KBr beam-splitter and a DTGS detector. The measurements were performed in vacuum at room temperature and spectra were recorded at 4 cm^{-1} resolution with 16 scans. Before the sample measurement a background reference was performed with an aluminum mirror placed at the same position as the sample. The normal thermal emittance, ε_{th}, was calculated as a weighted fraction between emitted radiation and the Planck black body distribution at a specific temperature (T) from the equation:

$$\varepsilon_{th} = \frac{\int_{1.6\mu m}^{25\mu m} I_{bb}(T,\lambda)[1-R(\lambda)]\, d\lambda}{\int_{1.6\mu m}^{25\mu m} I_{bb}(T,\lambda)\, d\lambda} \qquad (3)$$

where $I_{bb}(T,\lambda)$ is the temperature dependent spectral blackbody emissive power and $R(\lambda)$ is the spectral reflectance (whose temperature dependence is assumed to be negligible). Because the used measurement configuration doesn't allow to measure absolute reflectance, the original spectra are slightly overestimated (the reference Al mirror reflects less than 100%). The procedure to correct the data was to measure the reflectance of polished copper in the same conditions and determine the multiplying factor that gives room temperature emittance of 3%. Then all spectra were corrected by using the same multiplying constant.

3. Results and discussion

3.1 Optical properties of single layers

A series of individual thin layers based on $WSiAlN_x$ and $WSiAlO_yN_x$ were deposited with different nitrogen and oxygen partial pressures as reactive gases for 1 min on glass. $WSiAlN_x$ and $WSiAlOyN_x$ layers become more transparent and lose their metallic behavior as the nitrogen and oxygen partial pressures increase. This is mainly because of Al and Si nitrides and oxides, which are transparent. In accordance with this, the reflectance in the same wavelength range decreases with increasing nitrogen and oxygen partial pressures.

Fig. 1 shows the optical constants, refractive index (n) and extinction coefficient (k), as a function of wavelength in the range of 300 – 2500 nm, obtained from modeling of the experimental T and R spectra and for different partial pressures of reactive gases, as indicated in the legend of the figure. It shows the general behavior of n and k with a decrease as partial pressures of reactive gases increase for both nitride and oxynitride layers. Moreover, it is seen that the refractive indices for the $WSiAlN_x$ layers increase with the wavelength, which make these layers appropriate materials for selective absorption of solar radiation and other optical applications, because they can be used to enhance the solar absorption through the interference effect. Refractive indices and thicknesses of the bilayer structure should be chosen to obtain destructive interference at wavelengths around 0.5 μm and 1.3 μm, contributing to the decrease of the reflectance of the solar radiation and consequently improving its absorptance. An optical path length (product of the refractive index with the thickness, nd) of 1/4 wavelength (in a layer) would produce a net shift of 1/2 wavelength between the light reflected from the top surface and from the bottom interface, resulting in cancellation [17]. The increase of refractive index with the wavelength allows to have a broad range with high degree of destructive interference effect. The refractive index of $WSiAlO_yN_x$ layers also shows a similar behavior with wavelength, but for high partial pressures of working gases it becomes almost constant.

$WSiAlN_x$ has higher n and k than $WSiAlO_yN_x$ because it has higher metallic character. The increase of oxygen content, leads to the oxide formation, which have lower refractive index and extinction coefficient.
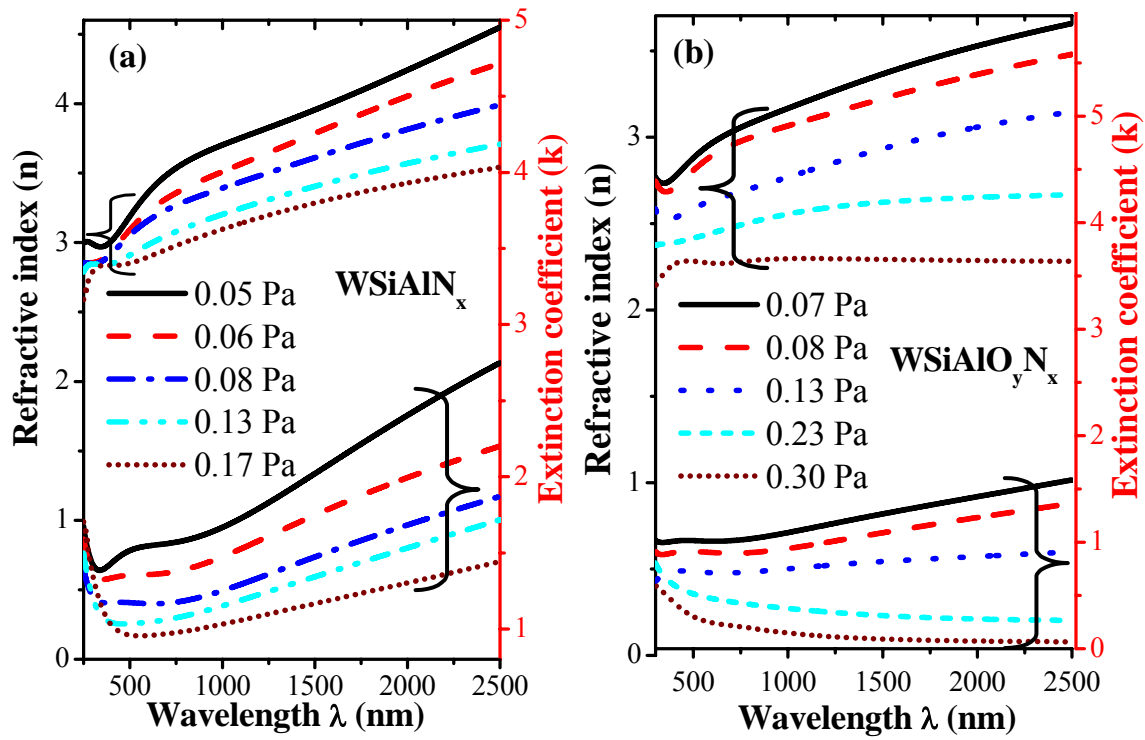
6

Fig. 1: Refractive index (*n*) and extinction coefficient (*k*) as a function of wavelength of: (a) WSiAlN$_x$, prepared with increasing nitrogen partial pressure. (b) WSiAlO$_y$N$_x$ as a function of wavelength, prepared with increasing nitrogen and oxygen partial pressures.

Elemental Tungsten and SiAlO$_x$ were chosen to be the back-reflector and the antireflection layer, respectively. Tungsten has a high temperature melting point and a high reflectance in IR region of radiation (R% = 94.6 at λ ~ 2.5 µm) as shown in Fig. 2a, which decreases the emissivity of the whole multilayer of the stack. Tungsten also contributes to energy absorption at solar radiation wavelength range, because of its reflectance in visible range. More information about optical constants (*n* and *k*) as a function of wavelength (λ) is shown in Fig. 2b.
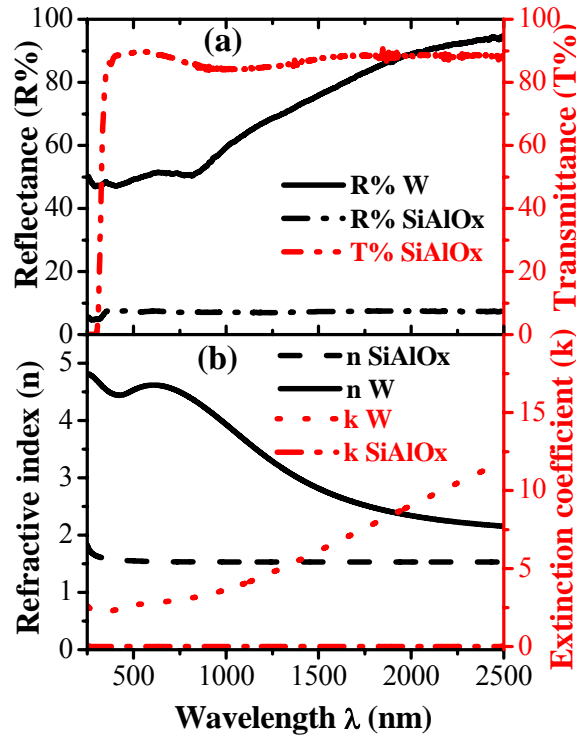
Fig. 2: a) Transmittance (T) and reflectance (R), b) refractive index (*n*) and extinction coefficient (*(n)*) of tungsten and SiAlO$_x$ layers.

On the other hand, the antireflection layer (SiAlO$_x$) is transparent and it has a low reflectance as shown in Fig. 2a. The extinction coefficient of this layer is very low (almost goes to zero), whereas it has a refractive index around 1.50, as shown in Fig. 2b. Moreover, it protects other layers against oxidation.

3.2 Chemical composition of single layers

The chemical composition of WSiAlN$_{P= 0.17 Pa}$, WSiAl(ON)$_{P= 0.30 Pa}$, SiAlO$_{P=0.062 Pa}$ thick layers, prepared in the same conditions of those used in the solar thermal absorber tandem are shown in Table I. EDS measurements were performed for two randomly chosen different positions for each sample and the average was calculated. A strong decrease of nitrogen and aluminum at% is seen in WSiAl(ON)$_{P= 0.30 Pa}$ coating comparing with WSiAlN$_{P= 0.17 Pa}$. Both are related with the oxygen addition as reactive gas. The induced target poisoning has a stronger effect on Al, decreasing its sputtering yield, what resulted in a decrease on Al content. These differences explain the decrement of WSiAl(ON)$_{P= 0.30 Pa}$ optical constants, the refractive index and extinction coefficient, *n* and *k*.

To assess the chemical states and bonding information of the films, the two single layers WSiAlN$_{P= 0.17 Pa}$ and WSiAl(ON)$_{P= 0.30 Pa}$ were prepared with the same parameters as those used in the multilayer stack and

were analyzed by XPS. Cores level spectra corresponding to W 4f, N 1s, Si 2p and Al 2s are shown in Fig. 3, whereas in Table II the Casa software fitting parameters and identification of core levels binding energies are represented. The W 4f core level was fitted into peak doublets with a spin-orbit energy separation as illustrated in section 2.2. Fig. 3a shows the W 4f core level spectra, where it is evident the presence of peaks of different tungsten oxide states. Those peaks were deconvoluted into four doublet components corresponding to W $4f_{5/2}$ and W $4f_{7/2}$. The peaks centered at 32.1, 33.1, 34.6, and 35.8 eV can be considered as W^{x+} (the intermediate W^{1+}, W^{2+} and W^{3+} oxidation states especially W-N in WN or W_2N compounds [18][19][20][21]), W^{4+}, W^{5+} and W^{6+} oxidation states of W $4f_{7/2}$, respectively. The same peaks corresponding to W $4f_{5/2}$ have an energy 2.18 eV higher, the assumed doublet spin-orbit separation. In nitride sample (WSiAlN$_{P= 0.17 Pa}$), elemental tungsten W $4f_{7/2}$ peak appears at 31.1 [13][22][23][24][25]. Elemental tungsten contributes to the solar radiation absorption in the visible wavelength range, which improve the absorption of whole stack.

As shown in Fig. 3b, the XPS spectra of N 1s core level can be deconvoluted into four peaks in both samples. The peaks centered at energies 397.0, 398.2 and 399.9 eV can be associated to W-N as WN or W_2N compounds [21][19][18][26], N-Si [27][28][29] and Si-O$_3$N or C = N [27][30][29], respectively. The fourth peak, at 401.9 eV, is considered as N – C = O surface contamination [30][31].

Fig. 5c shows the Si 2p core level spectra, where the sample WSiAlN$_{P= 0.17 Pa}$ has a contribution of three distinct components, whereas the WSiAl(ON)$_{P= 0.30 Pa}$ sample has two components. The two samples share peaks centered at 101.4 and 102.4 eV, recognized as Si - SiN$_3$ [21][28] and Si – N$_3$O or Si(Al)-SiO$_2$N [29] [30], respectively. The third peak that appears at 103.2 eV in sample WSiAlN$_{P= 0.17 Pa}$ is recognized as Si-O$_3$N as studied in more detail in [29]

Finally, Al 2s core level was used to obtain information from Al oxidation states, instead of Al 2p, because of the overlapping between W 5s and Al 2p core levels. Fig 3d shows the fitted Al 2s core level from both samples, which have one component centered at 116.6 eV that is related to Al – O bond energy [32]. Results obtained from XPS are very consistent with EDS analyses, especially the decrement in the amount of Al, Si and N in WSiAl(ON)$_{P= 0.30 Pa}$ sample comparing with WSiAlN$_{P= 0.17 Pa.}$ However, more oxygen was found in WSiAlN$_{P= 0.17 Pa}$ sample analyzed by XPS than the reported by EDS, which is normal because XPS is a surface analysis method (~ 5 nm) and there are more chances to find surface contamination.

The nitride has 27% of W atoms in the metallic oxidation state, 16 % in the W^{x+}, that can be associated to WN or W_2N, and 29 % in the W^{6+} oxidation state, whereas the oxynitride does not have W atoms in the

metallic oxidation state, 29 % in the W^{x+} and only 7 % in the W^{6+}. The amount of W^{6+} oxidation state in the nitride suggests its surface oxidation after the deposition, whereas the atoms in the metallic state are due to the low nitrogen partial pressure. The oxynitride was obtained increasing simultaneously the partial pressures of nitrogen and oxygen (ratio 85%: 15%), which justify the increase of the amount of W atoms in the oxidation state that can be addressed to WN or W_2N, and the decrease of W atoms in the metallic oxidation state. The oxygen partial pressure is still not enough to oxidize the W atoms in a high percentage.

Table I: Chemical composition of WSiAlN$_{P= 0.17 Pa}$, WSiAl(ON)$_{P= 0.30 Pa}$, and SiAlOx thick layers obtained by EDS analysis.

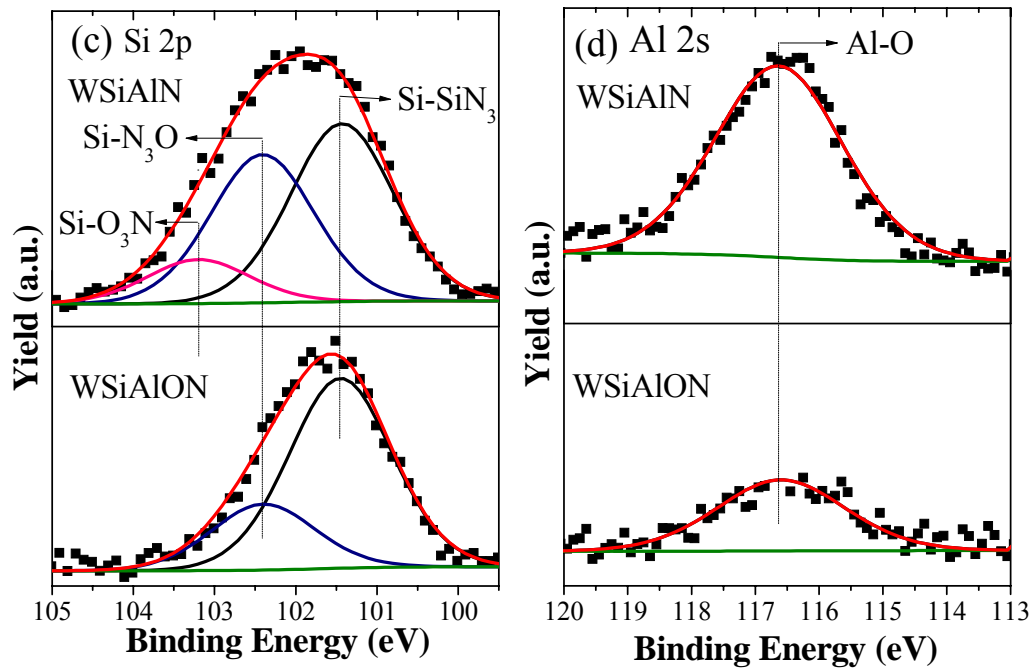| Layer	N at%	O At%	Al at%	Si at%	W at%	Ar at%
WAlSiN$_{P=0.17 Pa}$	29	3	13	20	33	2
WAlSi(ON)$_{P=0.30 Pa}$	25	27	3	16	29	-
SiAlO$_{P=0.06 Pa}$	-	63	11	25	-	1
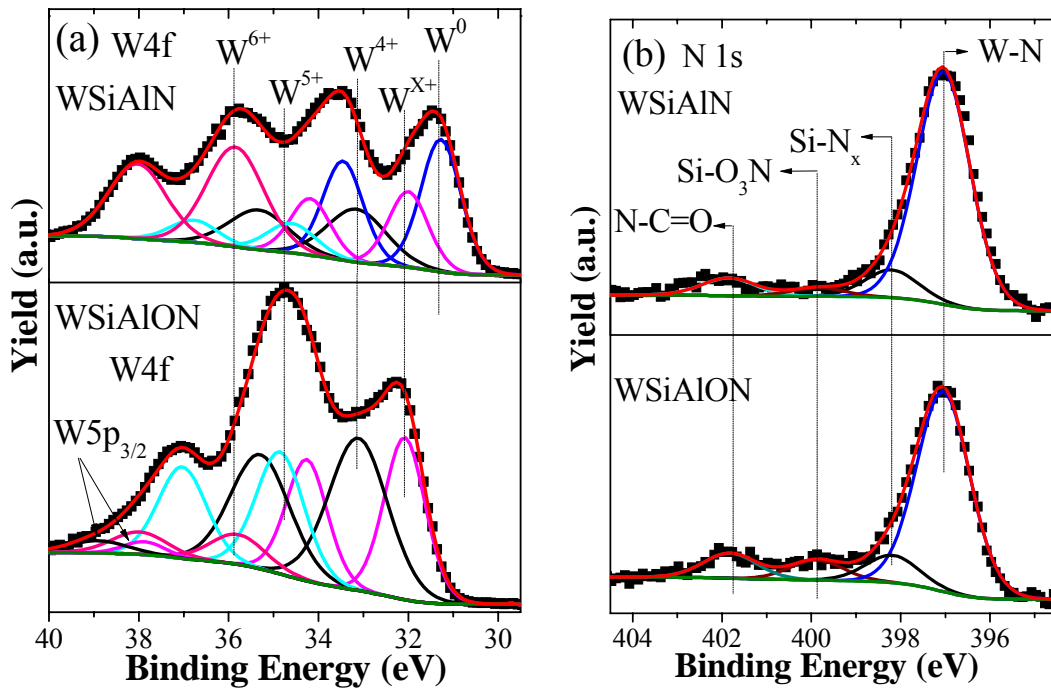
Fig. 3. XPS spectra of: (a) W 4f, (b) N 1s, (c) Si 2p, (d) Al 2s core level electrons for WSiAlN$_{P=0.17}$ $_{Pa}$ and WSiAl(ON)$_{P=0.30\ Pa}$ single layers. The green curve represents the background correction

Table II: Casa software fitting parameters and identification of core level binding energies.

Core Peak	FWHM (eV)	BE (eV) WSiAlN$_{P=0.17\ pa}$	BE(eV) WSiAl(ON)$_{P=0.30\ Pa}$	Compound or oxidation state
W 4f$_{7/2}$	1.1	31.1	-	W^0
	1.1	32.1	32.1	W^{x+}
	1.6	33.1	33.1	W^{4+}
	1.3	34.6	34.8	W^{5+}
	1.5	35.8	35.8	W^{6+}
N 1s	1.4	397.0	397.0	W-N
	1.4	398.2	398.2	N -Si
	1.4	399.9	399.9	Si-O$_3$N, C =N
	1.4	401.9	401.8	N-C =O
Si 2p	1.5	101.4	101.5	Si - SiN$_3$
	1.5	102.4	102.4	Si – N$_3$O or Si(Al)-SiO2N
	1.5	103.2	-	Si-O$_3$N
Al 2s	2.4	116.6	116.6	Al-O

3.3 Morphology and crystalline structure of single layers

XRD was performed for the single layers used in the absorber stack. As shown in Fig. 4, the diffractograms of $WSiAlN_{P= 0.17\ Pa}$, and $WSiAl(ON)_{P= 0.30\ Pa}$ layers show broad peaks, which is typical of materials with small grain size, whereas the $SiAlO_{P= 0.06\ Pa}$ layer does not show any feature, a characteristic of amorphous materials. The diffractogram of $WSiAlN_{P= 0.17\ Pa}$ shows a broad peak centred at the position of (110) plane of W α-phase (bcc), whereas the diffractogram of $WSiAl(ON)_{P= 0.30\ Pa}$ shows a broad peak centred at the position of (200) plane of W β- phase (A15 cubic). On the contrary, the diffractogram of W layer shows a combination of both α- and β- phases, but the α- phase is the dominant. So, W is polycrystalline with (110) orientation (2θ= 40º) [33][34]. Indeed, SEM cross sectional micrographs of thick single layers are completely agreeing with the XRD analysis, as shown in Fig. 5. The micrographs of $WSiAlN_{P= 0.17\ Pa}$, $WSiAl(ON)_{P= 0.30\ Pa}$ and $SiAlO_{P= 0.06\ Pa}$ layers show a featureless morphology, whereas for W layer a morphology typical of a columnar growth is present.
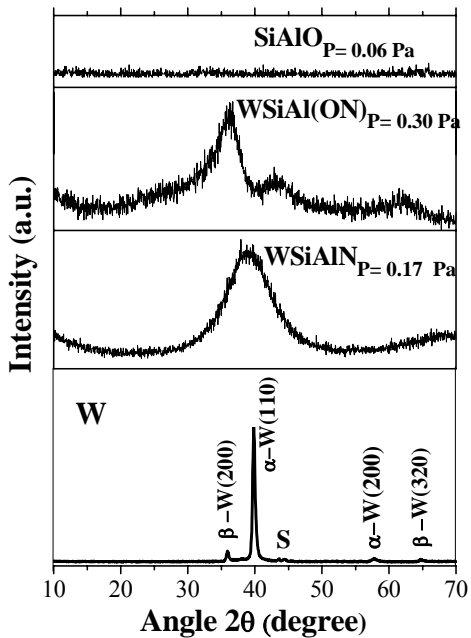

Fig. 4: XRD patterns of single layers performed with fixed incidence angle of $3^{°}$, from bottom to the top: W deposited on stainless steel, $WSiAlN_{P= 0.17\ Pa}$, $WSiAl(ON)_{P= 0.30\ Pa}$ and $SiAlO_{P= 0.06\ Pa,}$ layers deposited on stainless steel substrates (the peaks referenced by S correspond to stainless
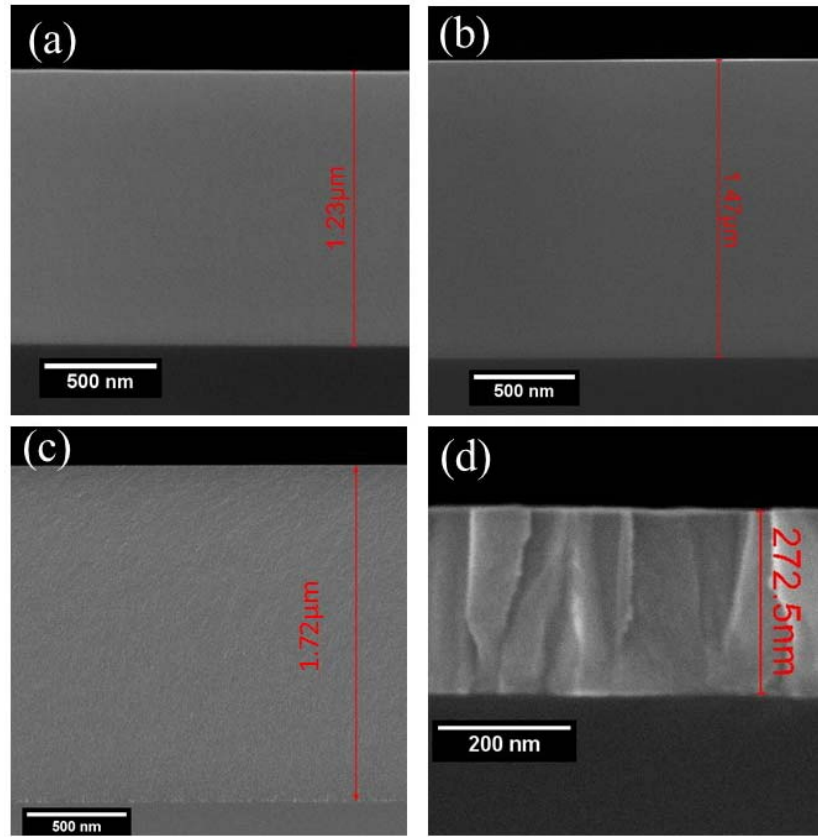
Fig. 5: Cross-sectional SEM micrographs of (a) WSiAlN$_{P= 0.17 Pa}$, (b) WSiAl(ON)$_{P= 0.30 Pa}$, (c) SiAlO$_{P=0.062}$ $_{Pa}$ and (d) Tungsten (W), thick single layers.

3.3 Design of the multilayer

Based on the data obtained from transmittance and reflectance of individual thin single layers, the multilayer was designed, modelled and optimized with SCOUT software. The optical constants (refractive index (n) and extinction coefficient (k)) and thicknesses, together with the corresponding partial pressures, are shown in Fig. 6a. The designed layers have a graded decreasing n and k from back-reflector W-layer towards the antireflection layer, as requested for efficient absorbers.

In Fig. 6b, it is shown how the whole stack was optimized by the addition of layers one by one. It is obvious that addition of multilayers results in an improvement upon the reflectance curve of the stack and upon the solar selectivity. This ensures that multilayers are adequate for more efficient solar absorbers.
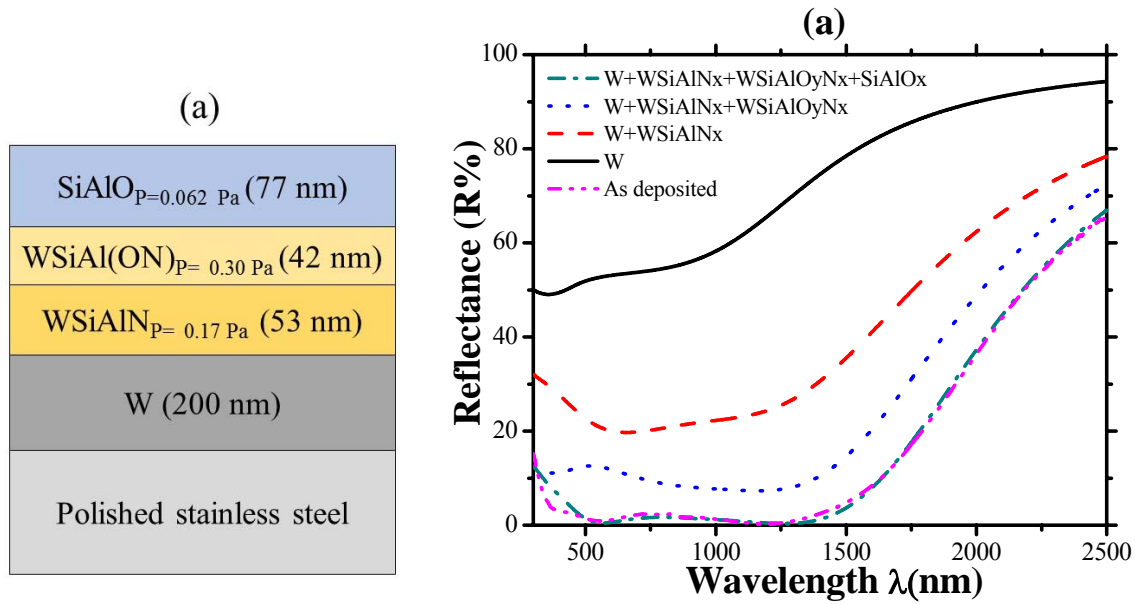
Fig. 6: (a) Schematic diagram of the simulated multilayer as obtained by SCOUT. (b) Simulated and experimental reflectance curves of the absorber design.

As shown in Fig. 6a, the optical stack is composed of four layers, the first is a back-reflector tungsten layer, that is followed by two absorption layers based on $WAlSiN_x$ / $WAlSiO_yN_x$ structure for phase interference. The final layer is an antireflection layer, which consists of $SiAlO_x$. The total simulated thickness of the whole multilayers absorber ($W/WAlSiN_x/WAlSiO_yN_x/SiAlO_x$) is ~ 372 nm. Fig. 6b also displays the reflectance curve of as deposited sample, that shows a good agreement with simulation, as expected. The final design shows simultaneously high solar absorptance, in average α= 96.2 %, and low emissivity, ε= 8.0 % (measured by emissometer at 80 ºC) and 9.8% calculated for 400 ºC using the IR reflectance in equation (3). Moreover, Fig. 7 shows a cross-sectional SEM micrograph of the optical stack, deposited on silicon substrate. W layer shows a typical morphology of a columnar growth type, whereas the remaining layers reveal a featureless morphology that completely agrees with XRD analysis of single layers. The total SEM thickness of as deposited tandem is about 367 nm, which is very close to simulated thickness taking into account the measurements error.
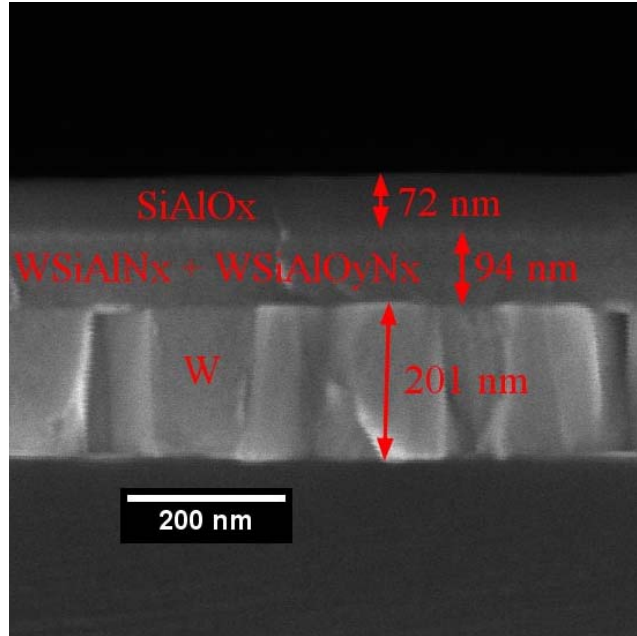
Fig. 7: Cross-sectional SEM micrograph of the optical stack, deposited on silicon substrate.

3.4 Thermal stability

For oxidation resistance and long term thermal stability, the solar absorber tandem was subjected to annealing tests in air, at 450 ºC, and in vacuum, at 600 ºC, for 400 h and 300 h, respectively. Then, absorptance (α) and thermal emittance (ε) were calculated, after each annealing step, from the reflectance curves by methods described in section 2.4. Fig. 8a represents the reflectance curves of as deposited sample, after 150 h and after 400 h of air annealing. The solar absorptance and thermal emittance at 400 ºC after each step are indicated in the legend of the figure. No notable changes are seen in the reflectance curve, solar absorptance and thermal emittance values. This means that the absorber stack showed a very good thermal stability when subjected to this air annealing. On the other hand, vacuum annealing was performed for 150 h and 300 h, as shown in Fig. 8b, that confirms very good thermal stability of the stack, also under vacuum. These results are very similar to those obtained with coating based on AlSiOx:W cermets with high (HA) and low (LA) metal volume fraction (W/AlSiO$_x$:W(HA)/AlSiO$_x$:W(LA)/AlSiO$_x$,)[35]. In the present work the annealing in vacuum was performed at 600 ºC, whereas in the previous one at 580 ºC. In the case of cermets, the absorption layers had a higher fraction of W atoms at metallic oxidation state, which were protected by the oxide matrix. In the present work, only the nitride has some W atoms at the metallic oxidation state, whereas the oxynitride layer has a big fraction of the W atoms with W-N bonds. In these samples the W content in absorption layers is around 30 at.%, whereas in the case of cermets absorption layers the W content is

15

below 20 at.% [35]. The difference is related with the fabrication process, because nitride and oxynitride layers could have less W, but in that case it would be necessary to deposit them with lower reactive gases partial pressure. In general, the emittance of the tandem was improved after first step of air and vacuum annealing. This means the IR absorption decreased and/or IR reflectance on W layer increased, showing that oxide and oxynitride layers protect the W layer against oxidation. These small changes can be due to the presence of some Si atoms in the $SiAlO_x$ antireflection layer, not oxidized at deposition stage [35], which were oxidized during the annealing steps. In the case of $AlSiO_x$:W cermets, two targets (W and AlSi) were used and to produce the nitride/oxynitride structure 3 targets (W, WSiAl and SiAl) were used. This procedure allowed to use, in the second case, a target with high Si content (in first case was Al prevailing) and to obtain an antireflection layer with lower refractive index. This can be one of the reasons the solar absorptance of nitride/oxynitride structure is slightly higher than cermet´s structure.
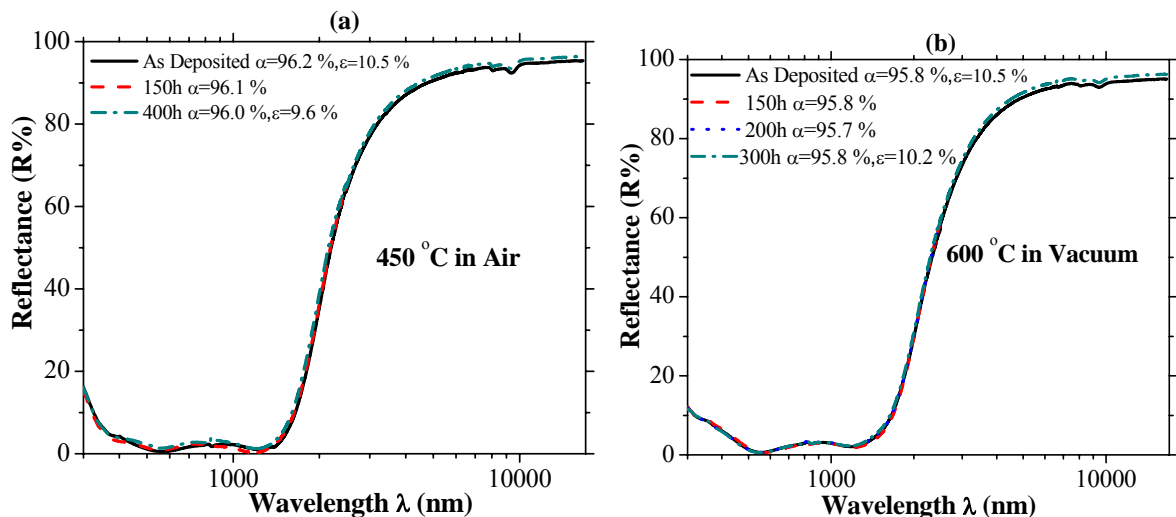

Fig. 8: Reflectance of as deposited optical stack and after (a) air thermal annealing at 400 ºC (b) vacuum thermal annealing at 600 ºC, with measured value of solar absorptance (α) and thermal emittance (ε) (calculated for 400 ºC).

In order to analyze if the tandem structure had been not changed or affected by oxidation after thermal treatment, the three samples (as deposited, after air and vacuum annealing) were analyzed by XRD. Fig. 9 represents the diffractograms of the three samples. As it is shown in the figure, results are completely agreeing with the one obtained from thick single layers that have a poor crystallinity, except the W layer, that is polycrystalline. However, there are no significant changes after the annealing, except small differences in the stainless steel peaks and in the intensity of W peaks. This confirms that the stack showed a good resistance against oxidation and it has a good thermal stability after annealing in air and vacuum at 450 ºC and 600 ºC, respectively.
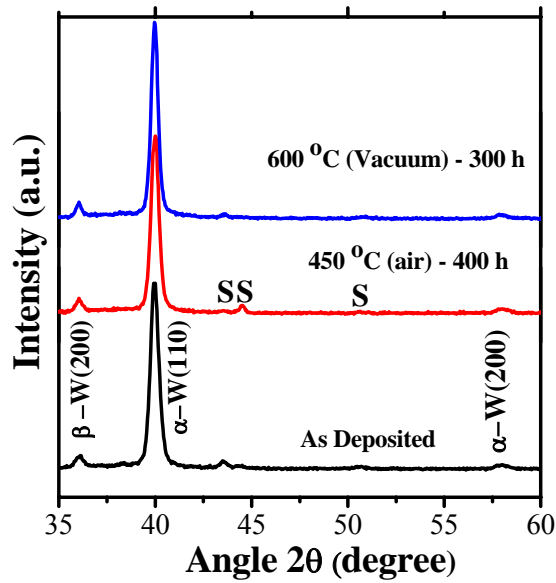
Fig. 9: X-ray diffraction of as deposited thermal absorber and after thermal annealing, as indicated in the legend. (the peaks referenced by S correspond to stainless steel as recorded by the previous study [35]).

4. Conclusions

A tandem coating for selective absorption of solar radiation for high temperature applications was fabricated by magnetron sputtering method. It is a multilayer based on four layers of structure ($W/WSiAlN_x/WSiAlO_yN_x/SiAlO_x$), as back reflector/high absorber/low absorber/antireflection layer, respectively. Thicker single layers of $WSiAlN_x$ and $WSiAlO_yN_x$ with the same coating parameters as those in the optical stack were used to study the structural, optical and chemical properties. These layers become more transparent and lose their metallic behavior with increasing nitrogen and oxygen partial pressures as reactive gases. As a result, the optical constants (refractive index and extinction coefficient, n and k) decreased. $WSiAlN_x$ has higher amount of Al, Si, N and W than $WSiAlO_yN_x$ as reported by EDS and XRD analysis. Moreover, XPS analysis prove the existence of tungsten in metal state, that may improve the solar absorptance of the tandem because of its contribution to the absorption in the visible solar radiation wavelength. On the basis of data from these single layers the tandem was initially simulated by the SCOUT software. The total thickness of the stack is ~ 367 nm as measured by SEM. Experimental design shows simultaneously high average solar absorptance, α=96.0%, and low emissivity, ε= 10% (400 ºC), together with high thermal stability at 450 ºC, in air and at 600 ºC, in vacuum, for 400 h and 300 h, respectively. After several steps of thermal annealing in vacuum and air annealing, the reflectance curve of the stack showed an excellent stability of the selectivity (α/ε) values, and there are no significant changes on the tandem reflectance curves. In most cases, thermal emissivity improved a bit, which implies that the W back reflector layer maintained its

17

reflectivity, meaning that it is well protected by the outermost layers. These results are very similar to those obtained with coating based on AlSiOx:W cermets with high and low metal volume fraction (W/AlSiO$_x$:W(HA)/AlSiO$_x$:W(LA)/AlSiO$_x$),

Finally, the WSiAlN$_x$, WSiAlO$_y$N$_x$ and SiAlO$_x$ layers show a featureless morphology, which is in accordance with the XRD amorphous like structure. On the contrary, tungsten layer W is polycrystalline with (110) orientation.

References
[1]   A. Fernández-García, E. Zarza, L. Valenzuela, M. Pérez, Parabolic-trough solar collectors and their applications, Renew. Sustain. Energy Rev. 14 (2010) 1695–1721. doi:10.1016/j.rser.2010.03.012.
[2]   S.D. Odeh, G.L. Morrison, M. Behnia, Modelling of parabolic trough direct steam generation solar collectors, 62 (1998) 395–406.
[3]   J. Ward, Modelling, optimisation and performance evaluation of a parabolic trough solar collector steam generation system, Sol. Energy. 60 (1997) 49–59.
[4]   L. Rebouta, P. Capela, M. Andritschky, A. Matilainen, P. Santilli, K. Pischow, E. Alves, Solar Energy Materials & Solar Cells Characterization of TiAlSiN / TiAlSiON / SiO 2 optical stack designed by modelling calculations for solar selective applications, Sol. Energy Mater. Sol. Cells. 105 (2012) 202–207. doi:10.1016/j.solmat.2012.06.011.
[5]   A. Soum-glaude, A. Le, M. Bichotte, C. Escape, L. Dubost, Solar Energy Materials and Solar Cells Optical characterization of TiAlN x / TiAlN y / Al 2 O 3 tandem solar selective absorber coatings, 170 (2017) 254–262. doi:10.1016/j.solmat.2017.06.007.
[6]   J. Jyothi, A. Soum-glaude, H.S. Nagaraja, H.C. Barshilia, Solar Energy Materials and Solar Cells Measurement of high temperature emissivity and photothermal conversion e ffi ciency of TiAlC / TiAlCN / TiAlSiCN / TiAlSiCO / TiAlSiO spectrally selective coating, Sol. Energy Mater. Sol. Cells. 171 (2017) 123–130. doi:10.1016/j.solmat.2017.06.057.
[7]   J. Feng, S. Zhang, Y. Lu, H. Yu, L. Kang, ScienceDirect The spectral selective absorbing characteristics and thermal stability of SS / TiAlN / TiAlSiN / Si 3 N 4 tandem absorber prepared by magnetron sputtering, 111 (2015) 350–356. doi:10.1016/j.solener.2014.11.005.
[8]   C. Zou, W. Xie, L. Shao, Functional multi-layer solar spectral selective absorbing coatings of AlCrSiN/AlCrSiON/AlCrO for high temperature applications, Sol. Energy Mater. Sol. Cells. 153 (2016) 9–17. doi:10.1016/j.solmat.2016.04.007.
[9]   A. Dan, J. Jyothi, K. Chattopadhyay, H.C. Barshilia, B. Basu, Solar Energy Materials & Solar Cells Spectrally selective absorber coating of WAlN / WAlON / Al 2 O 3 for solar thermal applications, Sol. Energy Mater. Sol. Cells. 157 (2016) 716–726. doi:10.1016/j.solmat.2016.07.018.

[10] Y. Wu, C. Wang, Y. Sun, Y. Ning, Y. Liu, Y. Xue, W. Wang, S. Zhao, E. Tomasella, ScienceDirect Study on the thermal stability of Al / NbTiSiN / NbTiSiON / SiO 2 solar selective absorbing coating, Sol. Energy. 119 (2015) 18–28. doi:10.1016/j.solener.2015.06.021.

[11] L. Rebouta, A. Sousa, M. Andritschky, F. Cerqueira, C.J. Tavares, P. Santilli, K. Pischow, Solar selective absorbing coatings based on AlSiN/AlSiON/AlSiOy layers, Appl. Surf. Sci. 356 (2015) 203–212. doi:10.1016/j.apsusc.2015.07.193.

[12] N. Fairely, CasaXPS Manual 2.3. 15, Casa Softw. Ltd. (2009) 1–177. http://scholar.google.com/scholar?hl=en&btnG=Search&q=intitle:CasaXPS+Manual+2.3. 15#2.

[13] F.Y. Xie, L. Gong, X. Liu, Y.T. Tao, W.H. Zhang, S.H. Chen, H. Meng, J. Chen, XPS studies on surface reduction of tungsten oxide nanowire film by Ar+ bombardment, J. Electron Spectros. Relat. Phenomena. 185 (2012) 112–118. doi:10.1016/j.elspec.2012.01.004.

[14] W. Theiss, SCOUT Thin Film Analysis Software Handbook, (2002).

[15] W.F. Bogaerts, Review materials for photothermal solar energy conversion, Mater. Sci. 18 (1983) 2847–2875.

[16] S.K.O. Leary, S.R. Johnson, P.K. Lim, The relationship between the distribution of electronic states and the optical absorption spectrum of an amorphous semiconductor : An empirical analysis The relationship between the distribution of electronic states and the optical absorption spectrum of, Appl. Phys. 3334 (1997). doi:10.1063/1.365643.

[17] Y. Yin, R.E. Collins, Optimization and analysis of solar selective surfaces with continuous and multilayer profiles, J. Appl. Physiscs. (1995). doi:10.1063/1.359124.

[18] X.X. Zhang, Y.Z. Wu, B. Mu, L. Qiao, W.X. Li, J.J. Li, P. Wang, Thermal stability of tungsten sub-nitride thin fi lm prepared by reactive magnetron sputtering, J. Nucl. Mater. 485 (2017) 1–7. doi:10.1016/j.jnucmat.2016.12.009.

[19] P. P´erez-Romo, C. Potvin, J.-M. Manoli, G. Dje'ga-Mariadassou, Phosphorus-Doped Tungsten Oxynitrides : Synthesis , Characterization , and Catalytic Behavior in Propene Hydrogenation and n-Heptane Isomerization, J. Catal. 205 (2002) 191–198. doi:10.1006/jcat.2001.3434.

[20] D. Cho, T. Chang, C. Shin, Variations in the surface structure and composition of tungsten oxynitride catalyst caused by exposure to air, Catal. Letters. 67 (2000) 163–169.

[21] C. Louro, A. Cavaleiro, F. Montemor, How is the chemical bonding of W   Si   N sputtered coatings ?, Surf. Coat. Technol. 142–144 (2001) 964–970. doi:10.1016/S0257-8972(01)01215-4.

[22] Y. Jiang, J.F. Yang, R. Liu, X.P. Wang, Q.F. Fang, Oxidation and corrosion resistance of WC coated tungsten fabricated by SPS carburization, J. Nucl. Mater. 450 (2014) 75–80. doi:10.1016/j.jnucmat.2013.05.050.

[23] E. Nanoscience, R. Azimirad, Influence of hydrogen reduction on growth of tungsten oxide nanowires, J. Exp. Nanosci. 7 (2012) 597–607. doi:10.1080/17458080.2011.551893.

[24] P. Uppachai, V. Harnchana, S. Pimanpang, V. Amornkitbamrung, A.P. Brown, R.M.D. Brydson, Electrochimica Acta A substoichiometric tungsten oxide catalyst provides a sustainable and ef fi cient counter electrode for dye-sensitized solar cells, Electrochim. Acta. 145 (2014) 27–33. doi:10.1016/j.electacta.2014.08.096.

[25] J. Zhang, J.P. Tu, X.H. Xia, Y. Qiao, Y. Lu, Solar Energy Materials & Solar Cells An all-

solid-state electrochromic device based on NiO / WO 3 complementary structure and solid hybrid polyelectrolyte, Sol. Energy Mater. Sol. Cells. 93 (2009) 1840–1845. doi:10.1016/j.solmat.2009.06.025.

[26] Y. Dong, J. Li, carbon black as efficient electrocatalysts for oxygen reduction reactions †, Chem. Commun. 51 (2014) 572–575. doi:10.1039/C4CC07137A.

[27] M. Rahman, S. Kamrul, Ellipsometric , XPS and FTIR study on SiCN films deposited by hot-wire chemical vapor deposition method, Mater. Sci. Semicond. Process. 42 (2016) 373–377. doi:10.1016/j.mssp.2015.11.006.

[28] G.M. Ingo, N. Zacchetti, D. Sala, C. Coluzza, Xray photoelectron spectroscopy investigation on the chemical structure of amorphous silicon nitride (aSiN x), J. Vac. Sci. Technol. 3048 (2014). doi:10.1116/1.576314.

[29] P. Cova, S. Poulin, O. Grenier, R.A. Masut, A method for the analysis of multiphase bonding structures in amorphous SiO x N y films, Appl. Phys. 73518 (2010). doi:10.1063/1.1881774.

[30] A. Al-rjoub, P. Costa, L. Rebouta, M.F. Cerqueira, P. Alpuim, N.P. Barradas, E. Alves, Surface & Coatings Technology Characterization of magnetron sputtered sub-stoichiometric CrAlSiN x and CrAlSiO y N x coatings, Surf. Coat. Technol. 328 (2017) 134–141. doi:10.1016/j.surfcoat.2017.08.038.

[31] H.J. Kim, I. Bae, S. Cho, J. Boo, B. Lee, J. Heo, I. Chung, Synthesis and characteristics of NH2- functionalized polymer films to align and immobilize DNA molecules, Nanoscale Res. Lett. 7 (2012) 30. doi:10.1186/1556-276X-7-30.

[32] N.H. Turner, A.M. Singlet, Determination of Peak Positions and Areas from Wide-scan XPS Spectra, Surf. Interface Anal. 15 (1990) 215–222.

[33] K.P. Sibin, S. John, H.C. Barshilia, Control of thermal emittance of stainless steel using sputtered tungsten thin films for solar thermal power applications, Sol. Energy Mater. Sol. Cells. 133 (2015) 1–7. doi:10.1016/j.solmat.2014.11.002.

[34] Y.G. Shen, Y.W. Mai, Influences of oxygen on the formation and stability of A15 b -W thin films, Mater. Sci. Eng. A. 284 (2006) 176–183.

[35] D. Dias, L. Rebouta, P. Costa, A. Al-rjoub, M. Benelmeki, C.J. Tavares, N.P. Barradas, E. Alves, P. Santilli, K. Pischow, Optical and structural analysis of solar selective absorbing coatings based on AlSiO x : W cermets, Sol. Energy. 150 (2017) 335–344. doi:10.1016/j.solener.2017.04.055.